Tsunamis generated by pyroclastic flows: experimental insights into the effect of the bulk flow density

Alexis Bougouin, Raphael Paris, Olivier Roche, Mathilde Siavelis, Andréa Pawlak Courdavault

To cite this version:

Alexis Bougouin, Raphael Paris, Olivier Roche, Mathilde Siavelis, Andréa Pawlak Courdavault. Tsunamis generated by pyroclastic flows: experimental insights into the effect of the bulk flow density. Bulletin of Volcanology, 2024, 86 (4), pp.35. 10.1007/s00445-024-01704-0 . hal-04509188

HAL Id: hal-04509188
https://hal.science/hal-04509188

Submitted on 18 Mar 2024

Tsunamis generated by pyroclastic flows: Experimental insights into the effect of the bulk flow density

Alexis Bougouin[1], Raphaël Paris[2], Olivier Roche[2], Mathilde Siavelis[2],
Andréa Pawlak Courdavault[2]

[1]Aix-Marseille Université, CNRS, IUSTI, Marseille, France.
[2] Université Clermont Auvergne, CNRS, IRD, OPGC, Laboratoire Magmas et Volcans,
Clermont-Ferrand, France.

*Corresponding author(s). E-mail(s): alexis.bougouin@univ-amu.com;
raphael.paris@uca.com;

Abstract

For a better assessment of hazards related to tsunamis triggered by pyroclastic flows entering water, it is crucial to know and quantify the contribution of the physical parameters involved in the generation of waves. For this purpose, we investigate experimentally the effect of pyroclastic flow density on tsunami generation by considering variably fluidized granular flows denser or less dense than water, referred to as heavy and light granular flows, respectively, by varying the particle density. Qualitative observations show that differences in bulk flow density mainly affect the propagation of granular flows underwater. In contrast, the bulk flow density has little effect on the amplitude of the leading and largest wave. In fact, the wave amplitude is initially similar to the local water depth along the inclined plane, and then reaches a maximum value that depends mainly on the other flow parameters (i.e., velocity, thickness, volume of flows). Far from the shoreline, we provide evidence of the bulk flow density effect on the wave amplitude, while other characteristics of the leading wave remain broadly unaffected in the range of parameters considered. Finally, a main difference on the tsunami generation between light and heavy granular flows is related to the energy distribution between the leading largest wave and the wave train, which is attributed to different modes of interaction of the two flow types with the water. For tsunami hazard assessment, our study suggests that the contribution of the bulk flow density on tsunami generation has a second-order effect compared to other flow parameters.

Keywords: tsunami, pyroclastic flow, bulk density, granular medium

1 Introduction

Pyroclastic density currents (PDCs) impacting a mass of water can trigger tsunamis (Day, 2015; Paris, 2015), as illustrated during the Santorini Minoan (Nomikou et al, 2016), Krakatau 1883 (Carey et al, 2000; Maeno and Imanura, 2011; Paris et al, 2014), Rabaul 1994 (Blong and McKee, 1995; Nishimura et al, 2005), Montserrat 1997 and 2003 (Pelinovsky et al, 2004; Mattioli et al, 2007), and Stromboli 2019 and 2021 (Giordano and De Astis, 2021; Casalbore et al, 2022) eruptions. PDCs are thought to be density-stratified and consist, in many cases, of a basal concentrated flow (called hereafter pyroclastic flow) with a particle concentration close to the maximum packing, topped by a dilute turbulent suspension

(Sulpizio et al, 2014; Dufek, 2016). In this regard, the density difference between the two parts of a PDC and the water is a fundamental ingredient in tsunami generation. While the upper dilute part can propagate above the water surface due to its low bulk density of the order of $1-10$ kg.m^{-3} (Carey et al, 1996), the behavior of the basal pyroclastic flow, with a bulk density close to that of water, is not clearly established. In fact, direct field measurements of the bulk density of pyroclastic flows represent a complex task because these flows are unpredictable, difficult to instrument, and often hidden by the upper dilute cloud. The density of unwelded pyroclastic flow deposits typically ranges between 800 and 1500 kg.m^{-3} (Schumacher and Mues-Schumacher, 1996; Milner et al, 2003), which suggests that weakly expanded parent flows are either denser (negatively-buoyant) or less dense (positively-buoyant) than water, referred to as heavy and light pyroclastic flows, respectively, in the following, due to the combined effect of density and porosity of the solid particles. It is thought that heavy pyroclastic flows can enter water, trigger waves (Watts and Waythomas, 2003), and then form underwater currents (Cas and Wright, 1991), or they can temporarily push back the shoreline at low angle of incidence (Legros and Druitt, 2000). In contrast, the behavior of light pyroclastic flows, for which the bulk density is lower, but of the same order as that of water, remains elusive. Can the flow temporarily enter water due to its inertia if the angle of incidence is not negligible? Can a tsunami be generated, and if so, are its characteristics similar to those triggered by heavy flows?

In order to answer these questions, we performed laboratory experiments that consist in generating a granular flow propagating along an inclined ramp, and then impacting a mass of water in a channel. The originality of the device used lies in the creation of fluidized granular flows (i.e., with gas pore pressure), which may propagate along an inclined plane with a slope angle significantly smaller than the angle of repose of granular materials, i.e. $\alpha_r \sim 25^\circ$ in our experiments. The dynamics of granular flows is usually quantified by the flow Froude number $Fr^f = u_f/(gh_f)^{1/2}$, where u_f and h_f are the velocity and thickness of the flow-front, respectively, and g is the gravitational acceleration. In the present experiments, the Froude number varies in the range $Fr^f = 10^0 - 10^1$, which is consistent with that of natural pyroclastic flows, i.e. $Fr^f = 10^{-1} - 10^1$ (Delannay et al, 2017). Recently, Bougouin et al (2020) showed that, for heavy granular flows at slope angles of $5-20^\circ$, the amplitude of the leading and largest wave far enough from the shoreline, normalized by the maximum water height H_o in the channel, depends on a single dimensionless parameter

$$\zeta = \left(\frac{u_f}{\sqrt{gH_o}}\right)\left(\frac{h_f}{H_o}\right)\left(\frac{\rho}{\rho_w}\frac{\upsilon}{{H_o}^2}\right)\sin\theta, \qquad (1)$$

where ρ and υ are the bulk density and the volume per unit width of granular flows, respectively, ρ_w is the water density, and θ is the slope angle of the inclined plane. Note that the term $\rho u_f h_f$ can be interpreted as the mass flux per unit width of the flow, and thus the morphology of waves is mostly controlled by the mass flux and the volume of granular flows (Bougouin et al, 2020). Moreover, each term in Equation (1) may be read as a dimensionless parameter, namely the Froude number $Fr = u_f/\sqrt{gH_o}$, the relative flow thickness $S = h_f/H_o$, the relative flow density $R = \rho/\rho_w$, and the relative flow volume $V = \upsilon/{H_o}^2$, as considered in previous empirical laws (Heller and Hager, 2010; Zitti et al, 2016). Moreover, the experiments of Bougouin et al (2020) showed that the amplitude of the leading and largest wave may be dependent on the size of grains, which controls the ability of water to percolate into the granular material, and thus the energy transfer from the granular flow to the water mass. More recently, such an effect of grain size on wave amplitudes was confirmed by combining laboratory experiments and numerical simulations in the case of non-fluidized sand masses falling into water (Lee and Huang, 2021). Experiments on fully-fluidized, bidisperse flows also revealed a slight decrease of the wave amplitude at decreasing volume fraction of fine particles typically smaller than 100 μm (Lipiejko et al, 2022).

In the present study, we investigate heavy (negatively-buoyant) and light (positively-buoyant) fine-grained flows with bulk densities that are of the same order of magnitude as the water density, but significantly different (i.e.,

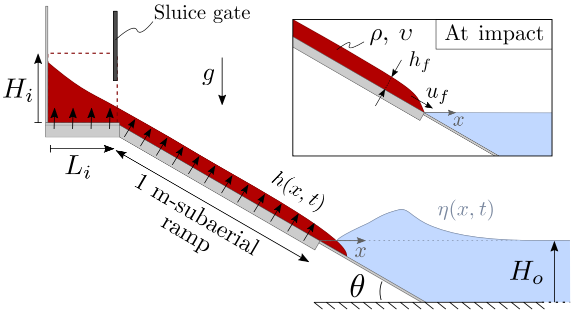

Fig. 1 Sketch of the experimental setup used in the present study.

$\rho \sim 600$ and $1500\,\mathrm{kg.m^{-3}}$), by varying the particle density. By contrast, Freundt (2003) and Allen et al (2012) did experiments with flows of ignimbrite ash (grains > 4 mm sieved off) whose estimated bulk density of $960 - 1000\,\mathrm{kg.m^{-3}}$ was very close to that of water, while Zweifel et al (2006) and Zitti et al (2016) realized experiments with granular flows of bulk density of 955 and $489\,\mathrm{kg.m^{-3}}$, respectively, but composed of coarse materials, i.e. $d \gtrsim 4\,\mathrm{mm}$. It therefore appears that the effect of the bulk flow density of fine-grained flows impacting water has not been investigated yet.

Hereafter, we present the results of our experiments and we show that heavy and light granular flows interact with the water in different ways, and resulting tsunamis can be distinguished accordingly. The paper is organized as follows. First, we introduce the experimental setup and materials used, followed by the general observations of the impact of heavy and light granular flows with water. Then, triggered waves are characterized with respect to the bulk flow density in the near- and far-field regions, respectively. Finally, we discuss our results in line with previous studies, and we highlight interests for the purpose of tsunami hazard assessment.

2 Experimental setup

Laboratory experiments are performed in a horizontal transparent channel of rectangular-cross section with dimensions of 7 m long, 0.8 m high, and 0.2 m wide. They consist in generating a granular flow by quickly releasing an initial column of grains, characterized by a constant volume (per unit width) of length $L_i = 33.8 \pm 0.1$ cm and height $H_i = 21 \pm 1$ cm for all experiments, along an inclined plane at $\theta = 15^\circ$ or 30°, before the flow enters fresh water with a maximum depth of $H_o = 26.5 \pm 0.2$ cm (Fig. 1). The thickness profile of the granular flow $h(x,\,t)$ and the water height elevation $\eta(x,\,t)$ are recorded using two Photron Fastcam 1024 × 1024 pixels video cameras with a spatial resolution of 4 mm/pixel (wide view) and 0.8 mm/pixel (water height elevation recorded between $x = 2$ and 2.8 m from the shoreline), and an acquisition rate of 250 Hz. As these experiments require time to be performed, reproducibility is assessed from two experiments providing a variability of about $10 - 15\%$ on the amplitude of the leading wave. More details on the experimental setup can be found in Bougouin et al (2020, 2021).

The originality of this device lies in the ability to control the degree of fluidization of the granular material in the reservoir and along the 1 m-subaerial ramp (see black arrows representing the air flux, in Fig. 1). The degree of fluidization allows to vary the main flow parameters (Fig. 2), namely the volume per unit width υ entering water, the velocity u_f and the thickness h_f of the flow-front at the impact, each of them controlling the tsunami generation. For this reason, we consider the degree of fluidization $\beta = V_f/V_{mf}$, which compares the air velocity V_f to the minimum fluidization velocity V_{mf} of granular materials, ranging from 0 (non-fluidized) to 1.3 (fully-fluidized), in the present study. Note that no significant variation in the initial volume fraction ϕ_i of granular columns is reported by varying β, so that the volume and mass of granular columns are equal for all experiments performed with the same granular material. Furthermore, the volume fraction is not expected to vary significantly during the flow emplacement, thus causing no bulk flow density variation.

Overall, the increase of β increases both the granular-to-water velocity ratio u_f/u_f^W [Fig. 2(a)] and thickness ratio h_f/h_f^W [Fig. 2(b)], where u_f^W and h_f^W are the velocity and thickness of water flow-fronts under conditions similar to those of granular flows. At large β, both u_f/u_f^W and h_f/h_f^W reach a constant value of 1 (solid line), which is consistent with the decrease of frictional dissipation within the granular flows that behave like weakly-dissipative water flows (Roche et al, 2008). At small β, a greater dispersion of data is

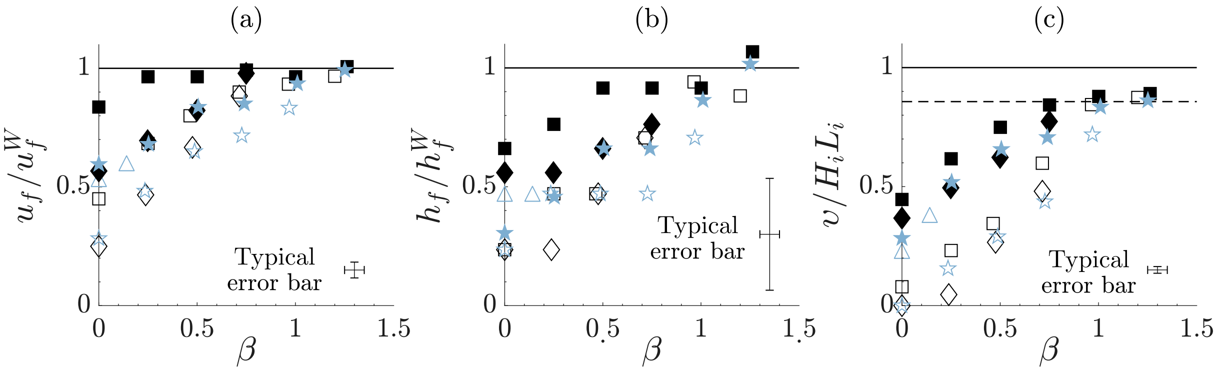

Fig. 2 Granular-to-water flow-front (a) velocity ratio u_f/u_f^W and (b) thickness ratio h_f/h_f^W, and (c) fraction of the total volume υ/H_iL_i of granular flows entering water, as a function of the degree of fluidization β. (—) value of 1; (- - -) $\upsilon/H_iL_i = 1 - h_l/H_i$, which corresponds to no deposit along the subaerial inclined plane and a granular layer of $h_l = 3$ cm on the horizontal bottom of the reservoir, at the end of the experiments. Symbols: (□) G66; (◇) G159; (☆) P143; (△) P580, with slope angles of $\theta = 15°$ (opened) and $\theta = 30°$ (closed). Error bars are based on the accuracy of measurements.

reported due to the effect of slope angle and grain diameter, possibly because of self-fluidization during the collapse of granular columns on inclined planes. The fraction of the total volume υ/H_iL_i that entered the water is also shown to increase with increasing β up to a value smaller than one [dashed line vs. solid line, in Fig. 2(c)] because some grains remain on the horizontal bottom of the reservoir.

To investigate heavy and light pyroclastic flows, we considered particles of different densities, while their size and shape are well controlled. We used spherical, quasi-monodisperse, glass beads of mean diameter $d = 66$ μm or $d = 159$ μm with a density of $\rho_p = 2500$ kg.m^{-3} (listed as G66 and G159, respectively), or spherical, quasi-monodisperse, polystyrene beads of mean diameter $d = 143$ μm or $d = 580$ μm with a density of $\rho_p = 1050$ kg.m^{-3} (listed as P143 and P580, respectively). Grain size is selected to ensure that full homogeneous fluidization of granular columns can be obtained in this device, and in this regard we do not consider neither coarse glass beads that require air fluxes that are too high nor small polystyrene beads sensitive to cohesive forces. More details on the grain characteristics (e.g., size distribution, minimum fluidization velocity, friction angles) and a summary table of all experiments are provided in the Supporting Information.

Considering that the length scales of laboratory experiments and natural cases are different, the orders of magnitude of relevant dimensionless parameters controlling the tsunami generation are now discussed. The tsunami generation process is mainly governed by four dimensionless parameters, namely the Froude number $Fr = u_f/(gH_o)^{1/2}$, the relative flow thickness $S = h_f/H_o$, the relative flow density $R = \rho/\rho_w$, and the relative flow volume $V = \upsilon/H_o^2$ (Fritz et al, 2004; Zweifel et al, 2006; Heller and Hager, 2010; Zitti et al, 2016; Bullard et al, 2019a; Bougouin et al, 2020; Lipiejko et al, 2023). Here, these parameters are in the range $Fr = [0.9 : 2.2]$, $S = [0.02 : 0.08]$, $R = [0.6 : 1.5]$ (the bulk flow density ρ is estimated from the volume fraction ϕ_i of initial granular columns), and $V = [0.05 : 0.93]$, respectively. With the experimental conditions chosen, it is possible to investigate granular flows lighter ($R < 1$) or heavier ($R > 1$) than fresh water through the variation in particle density, which is the main scope of this study. Note, however, that the grain to water density ratio ρ_p/ρ_w is strictly larger than one, which does not permit us to address pumice rafts on the water surface as observed in the field (Jutzeler et al, 2014).

3 General observations

The typical behavior of a (a) light (positively-buoyant) and (b) heavy (negatively-buoyant) granular flows entering water is shown in Fig. 3, at different times after gate opening. Movies of the same experiments are also available in the Supporting Information.

Shortly after the impact, the water body is pushed by the granular flow entering water and

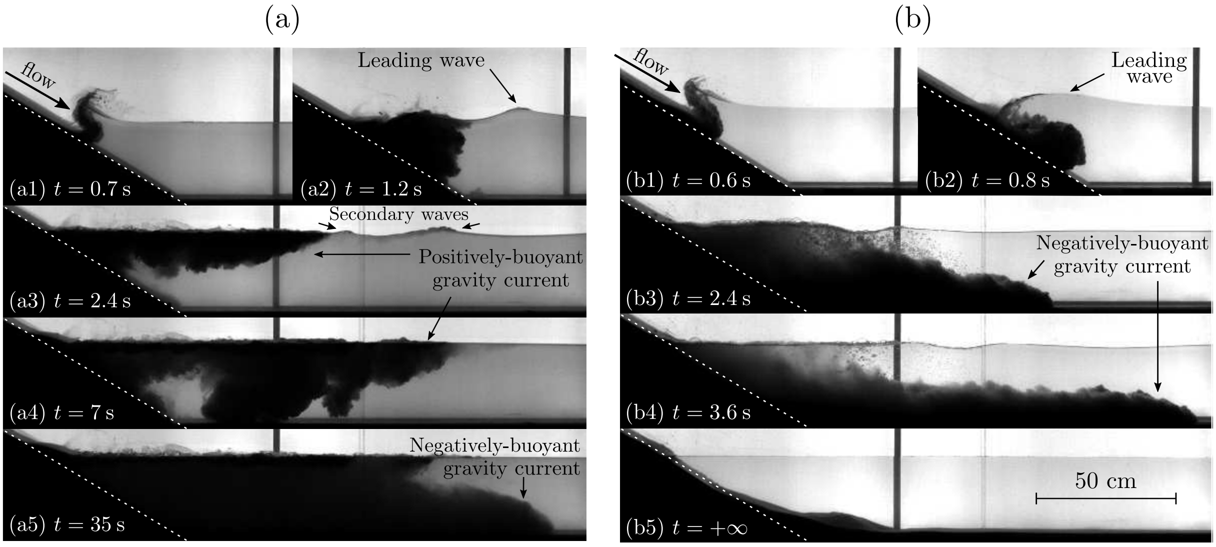

Fig. 3 Snapshots of a (a) light (particles P143) or (b) heavy (particles G159) granular flow entering water, at different times after gate opening. The degree of fluidization and the slope angle are set to $\beta = 0.75$ and $\theta = 30^\circ$, respectively.

the water height elevation rises locally [Figs 3(a1) and 3(b1)]. At the same time, a small volume of grains may be ejected above the water surface [Fig. 3(a1)], thus forming a granular jet (Bougouin et al, 2021), but most grains penetrate the water forming a turbulent mixing zone underwater, regardless of the flow type [Figs 3(a2) and 3(b2)]. Then, the turbulent mixing zone evolves according to the initial density of the granular flows, while a first wave, which is also the largest one, is generated and propagates freely away. For light granular flows, the turbulent mixing zone rises to form a positively-buoyant gravity current traveling along the water surface [Figs. 3(a3) and 3(a4)]. Although the grains are denser than water, the positively-buoyant dynamics suggests that initially a sufficient amount of air remains trapped in the granular material. In addition, small-amplitude waves appear behind the leading wave, which ends approximatively when the current stops at a finite length along the water surface. At longer times, grains fall into the water to form a negatively-buoyant gravity current that propagates along the bottom of the tank [Fig. 3(a5)]. In contrast, heavy granular flows propagate solely as negatively-buoyant gravity currents underwater [Fig. 3(b3) and 3(b4)], from which the interstitial air escapes as numerous bubbles rapidly after granular flow enters the water [Fig. 3(b3)]. Finally, at sufficiently long times, both flow types form underwater deposits, which are characterized by a large volume of grains at the slope break and a thin granular layer along the bottom of the tank [see Fig. 3(b5)]. While the effect of the bulk flow density on the granular dynamics underwater is clearly established, we aim to quantify its influence on the tsunami generation in the following.

4 Generation of the leading wave

A first way to characterize the effect of the bulk flow density on tsunami generation consists in tracking, shortly after the impact, the amplitude A of the leading and largest wave as a function of its position x^A from the shoreline, as shown in Fig. 4(b). As long as the leading wave is forced by the granular flow, the wave amplitude corresponds to the maximum water height elevation located at the granular-water interface [see Fig. 3(a1)-(b1)]. During this stage, the wave amplitude A increases quasi-linearly with its position, i.e. $A/H_o \propto x^A/H_o$ [Fig. 4(b)]. Two trends can be clearly distinguished depending on the slope angle θ of the inclined plane. At first order, it can be argued that, during the generation process, the triangular-shaped water body in contact with the inclined plane, initially below the undisturbed water surface, is pushed by the granular flow and

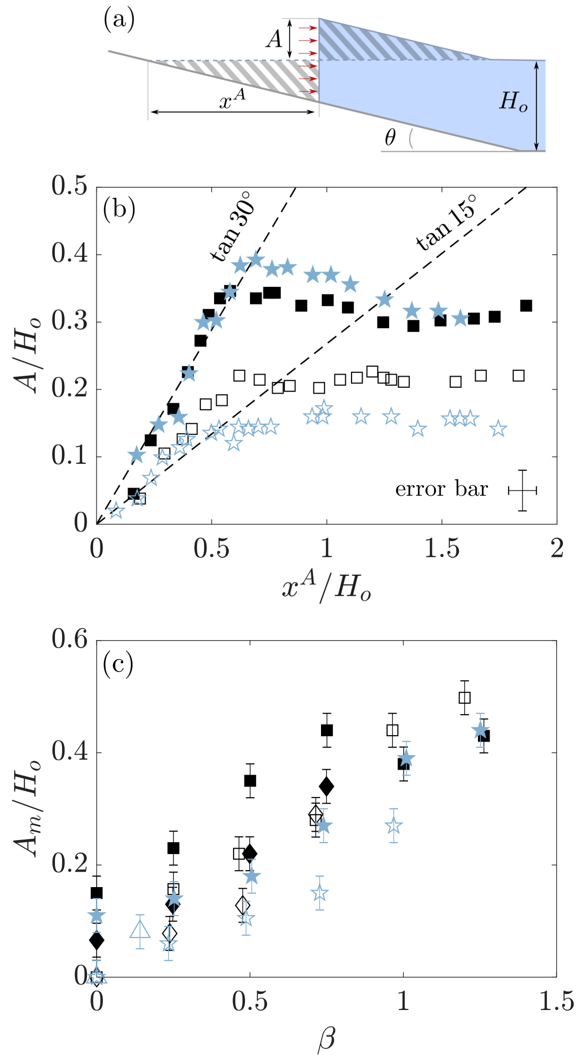

Fig. 4 (a) Sketch of the leading wave generation at impact, during which the triangular-shaped water body, initially below the undisturbed water surface, is pushed by the granular flow (red arrows) above the water surface. (b) Scaled amplitude A/H_o of the leading wave versus its scaled position x^A/H_o from the shoreline, for heavy granular flows (particles G66) - (□) $\beta = 0.5$, $\theta = 15^\circ$; (■) $\beta = 0.5$, $\theta = 30^\circ$ - and light granular flows (particles P143) - (☆) $\beta = 0.75$, $\theta = 15^\circ$; (★) $\beta = 1$, $\theta = 30^\circ$ - entering water. (- - -) $A/H_o = x^A \tan\theta/H_o$. (c) Maximum-scaled amplitude A_m/H_o of the leading wave versus the degree of fluidization β. Symbols: (□) G66; (◇) G159; (☆) P143; (△) P580, with $\theta = 15^\circ$ (opened) and $\theta = 30^\circ$ (closed). Error bars are based on the accuracy of measurements.

it is displaced, without significant modifications of the initial shape, above the water surface [Fig. 4(a)]. To support this statement, dashed lines in Fig. 4(b) show the relation $A/H_o = x^A \tan\theta/H_o$, corresponding to the equality between the wave amplitude and the local water depth, which is in fairly good agreement with experimental data up to a critical value of x^A/H_o depending on initial conditions. When data deviate from this trend, the maximum amplitude A_m of the leading wave is reached, and the generation process is therefore ended. As a consequence, the leading wave propagates freely far away with an amplitude remaining fairly constant for bore waves and slightly decreasing for solitary-like waves observed at $\theta = 15^\circ$ and $\theta = 30^\circ$, respectively, at early times of the propagation.

As the leading and largest wave shows typical behavior in all experiments during the generation process, the effect of the bulk flow density is mainly seen in the maximum amplitude A_m reached at the end of the wave generation. More specifically, Fig. 4(c) shows the maximum-scaled amplitude A_m/H_o as a function of the degree of fluidization β, for heavy (black symbols) and light (blue symbols) granular flows with $\theta = 15^\circ$ (opened symbols) and $\theta = 30^\circ$ (closed symbols). Note that, for a given β and θ, flow parameters, namely the front velocity u_f, the front thickness h_f, and the volume per unit width v of granular flows, are found to be close for the different materials used, and particularly for particles P143 and G159 (Fig. 2). As expected, the maximum-scaled amplitude A_m/H_o increases with the degree of fluidization β and the slope angle θ, both promoting a higher mobility of granular flows. Beyond the general trend, the maximum-scaled amplitude A_m/H_o is slightly lower for waves generated by light granular flows (blue symbols) than for those generated by heavy granular flows (black symbols) entering water. However, the influence of the bulk flow density is less than that of β, in the range of parameters considered here.

5 Far-field characterization of the waves

In order to further investigate the effect, albeit moderate, of the bulk flow density on tsunami generation, we consider the water height elevation far away from the shoreline, where an estimate of wave properties can be more accurate.

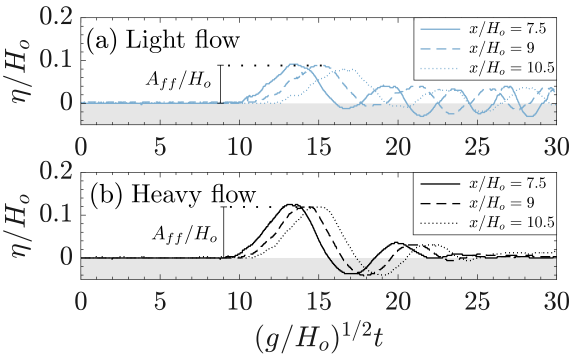

Fig. 5 Temporal evolution of the water height profile η/H_o disturbed by a (a) light (particle P143) and (b) heavy (particle G159) granular flow ($\beta = 0.5$, $\theta = 30^\circ$) entering water, at different positions from the shoreline.

5.1 Water height evolution

Figure 5 shows the temporal evolution of the water height elevation η/H_o disturbed by (a) light and (b) heavy granular flows entering water, at $x/H_o = 7.5$, 9 and 10.5 from the shoreline. Here, the degree of fluidization and the slope angle are set to $\beta = 0.5$ and $\theta = 30^\circ$, leading to a Froude number of $Fr = 1.8$, a relative flow thickness of $S = 0.05$, and a relative flow volume of $V = 0.64$, for both flow types. The relative flow density R is therefore the unique dimensionless parameter varied here, with (a) $R = 0.6$ and (b) $R = 1.4$, respectively.

As expected for subaerial mass flows impacting water, the initial disturbance of the water surface corresponds first to a positive crest, namely the leading and largest wave, followed by a lower trough. Our results reveal the physical contribution of the bulk flow density on tsunami generation in the far-field region, with a slightly lower amplitude of the leading wave generated by light granular flows compared to heavy granular flows (Fig. 5). Moreover, the number of waves contained in the wave train behind the leading wave increases significantly with decreasing the bulk flow density that reveals a different interaction between the granular material and the water surface, as discussed later.

5.2 Far-field amplitude of the leading wave

Quantitatively, the bulk flow density has more effect on the far-field amplitude A_{ff} than on the maximum amplitude A_m of the leading wave near the shoreline [Fig. 6(a) vs. Fig. 4(c)], while no effect is observed for other wave features (see Appendix). At a given β, an increase of A_{ff}/H_o by a factor of about 2.7 [Fig. 6(a)], compared to a gross factor of about 2 for A_m/H_o [Fig. 4(c)], is observed by increasing the bulk density with a factor 2.4. This suggests a different decay of the wave amplitude from the near- to far-field regions, which is clearly shown by the amplitude ratio A_m/A_{ff} decreasing approximatively from 3 to 2 for light granular flows (blue), and from 2 to 1 for heavy granular flows (black), with increasing β [Fig. 6(b)]. However, it is not clear that this result can be only attributed to the variation of the bulk flow density, or more precisely, to the positively/negatively-buoyant dynamics of granular flows underwater. Note that, for a given bulk flow density, the small decrease of A_m/A_{ff} with β is due to the fact that low-amplitude waves, obtained at low β, are generated closer to the shoreline compared to large-amplitude waves, obtained at large β.

Another interesting outcome is that the change in bulk flow density is well captured by the scaling of Bougouin et al (2020) that predicts the scaled amplitude A_{ff}/H_o of the leading wave, estimated at $x = 2.4$ m from the shoreline (corresponding here to $x/H_o = 9$), as a function of a unique dimensionless parameter $\zeta = FrSRV \sin\theta$ (Eq. 1) [Fig. 6(c)]. At large ζ, all data collapse on a master curve $A_{ff}/H_o = \zeta^{2/7} \propto 1/H_o$ (- - -), which suggests that the wave amplitude is independent on the maximum water depth H_o. At low ζ, it is found a linear trend as $A_{ff}/H_o \propto \zeta$ (—), with a prefactor equal to 4 or 16 with $\theta = 30^\circ$ or 15°, respectively. Note that all data of Bougouin et al (2020) with $\theta = 5$, 10 and 20° are in agreement with the trend $A_{ff}/H_o = \zeta^{2/7}$ (- - -), which appears to account for the effect of the slope angle. We emphasize that the robustness of this scaling law is now demonstrated for various front velocities $u_f = [0.75 : 4.1]\,\mathrm{m.s^{-1}}$, front thicknesses $h_f = [0.6 : 3.5]$ cm, volumes per unit width $\upsilon = [0.3 : 13.9] \times 10^{-2}\,\mathrm{m^2}$, bulk flow densities $\rho = [589 : 1481]\mathrm{kg.m^{-3}}$, slope angles $\theta = [5 : 30]^\circ$, and water depths $H_o = [13.1 : 38.5]$ cm, corresponding to a wide range of Froude number $Fr = [0.9 : 3.2]$, relative flow thickness $S = [0.015 : 0.18]$, relative flow volume $V = [0.05 : 5.3]$, and relative flow density $R = [0.6 : 1.5]$. This scaling also holds for

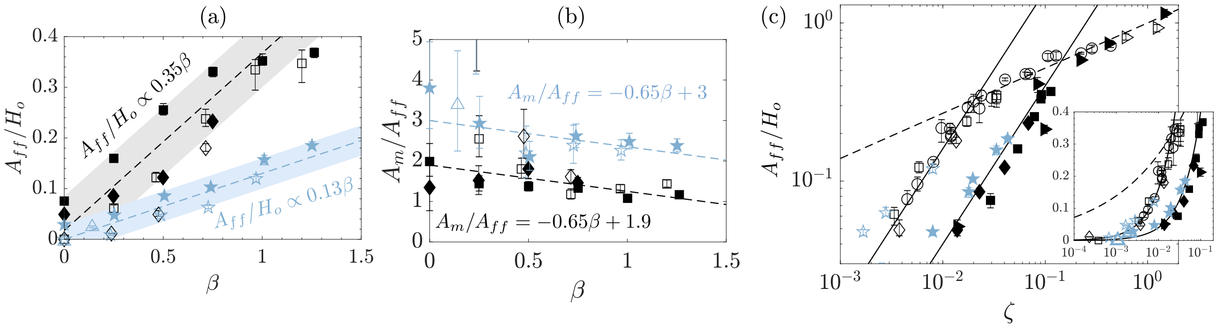

Fig. 6 (a) Scaled far-field amplitude A_{ff}/H_o and (b) maximum to far-field amplitude ratio A_m/A_{ff} of the leading wave versus β. Note that A_{ff} is estimated at $x = 2.4\,\mathrm{m}$ (i.e., $x/H_o = 9$) from the shoreline, while error bars indicate the variation from $x = 2$ to $2.8\,\mathrm{m}$ (i.e., from $x/H_o = 7.5$ to 10.5). (c) A_{ff}/H_o versus ζ (Eq. 1) in log-log representation (inset: lin-log representation). Symbols: (□) G66; (◇) G159; (☆) P143; (△) P580, with $\theta = 15^\circ$ (opened) and $\theta = 30^\circ$ (closed); (▷) additional experiments (see SI) and (○) Data of Bougouin et al (2020), with $\theta \leq 20^\circ$ (opened) and $\theta = 30^\circ$ (closed).

various grain diameters $d = [65 : 500]\,\mu$m (note that different prefactors found for millimeter-sized grains in Bougouin et al (2020) was attributed to the flow permeability), degree of fluidization $\beta = [0 : 1.3]$, and nature of the flowing materials (i.e., water and granular flows). Nonetheless, further work is now required to understand better the physical origin of this scaling.

5.3 Energy transfer

The influence of the bulk flow density on tsunami generation is also highlighted by the wave train behind the first positive crest (Fig. 5). More specifically, for light granular flows entering water, successive low-amplitude waves are observed behind the leading wave, which are not reported for heavy granular flows. This suggests different interactions between light or heavy granular flows and the water, which could be attributed to the role of escaping gas and/or sinking of the negatively-buoyant flow, both of which are related to the penetration of water into the granular material. Another cause may be the balance between flow inertia and buoyancy that leads to oscillating dynamics around the water surface, like a disturbed float. It is difficult to draw clear conclusions from these experiments, but this observation gives insight into the effect of bulk flow density.

For quantifying the importance of the leading wave with respect to the total wave train, Fig. 7 shows the energy $\langle E_w \rangle$ of the leading wave crest as a function of the energy E_w of the total wave train, scaled by the kinetic energy E_k^f of the granular flow (see bottom inset, Fig. 7). Here, the leading wave energy, the total wave energy and the kinetic granular flow energy are defined per unit width, respectively, as

$$\langle E_w \rangle = \rho_w g c \int_0^T \eta^2 dt, \qquad (2)$$

$$E_w = \rho_w g c \int_0^\infty \eta^2 dt, \qquad (3)$$

$$E_k^f = \frac{1}{2} \rho \upsilon {u_f}^2, \qquad (4)$$

where T is the period of the first positive crest, and $c = (gH_o)^{1/2}$ is the wave velocity (see Appendix). Note that the relations used for $\langle E_w \rangle$ and E_w assume an equipartition of potential and kinetic energies of the disturbed free-surface, which holds true for linear waves (Le Méhauté, 1976) and is a reasonable assumption for impulse waves far enough from the shoreline (Fritz et al, 2004; Zitti et al, 2016). Thus, Equations 2 and 3 are only twice the potential energy (per unit width) of an elementary volume of water integrated over the volume of the leading wave crest and that of the total wave train, respectively.

Figure 7 shows that the total wave energy E_w, as well as the leading wave energy $\langle E_w \rangle$, represents about 1 to 10% of the kinetic energy E_k^f of the granular flow, i.e. $E_w/E_k^f = [0.01 : 0.1]$, in the range of parameters considered, which is consistent with common values found in the literature (Viroulet et al, 2014; Zitti et al, 2016; Clous and Abadie, 2019). Moreover, most of the total wave energy is contained in the first positive crest, even though slightly differing from the slope 1 (solid

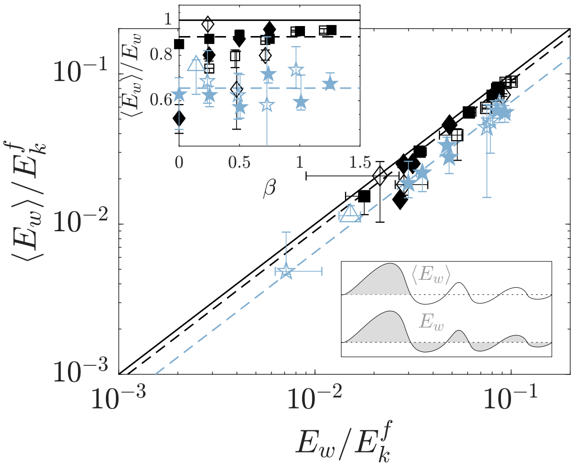

Fig. 7 Energy of the leading wave crest $\langle E_w\rangle$ as a function of the total wave energy E_w, scaled by the kinetic energy E_k^f of light (blue) and heavy (black) granular flows (Top inset : $\langle E_w\rangle/E_w$ versus β). (—) 100%, (- - -) 90% (black) and 65% (blue) of the total wave energy is contained in the leading wave. Symbols: (□) G66; (◇) G159; (☆) P143; (△) P580, with $\theta = 15^\circ$ (opened) and $\theta = 30^\circ$ (closed). Error bars are based on the accuracy of measurements.

line), i.e. $\langle E_w\rangle = E_w$. Our results also reveal differences in energy repartition between the two flow types (dashed lines), which is related to different modes of interaction between light or heavy granular flows and the water. More quantitatively, our results show that 90% (black dashed line) and 65% (blue dashed line) of the total wave energy is contained in the leading wave, for heavy and light granular flows entering water, respectively. In the top inset of Fig. 7, this difference in energy transfer is clearly observed at large β, while, at low β, data are more scattered probably because relatively slow heavy granular flows triggered several low-amplitude waves after the leading wave. In summary, it appears that the temporal evolution of the water surface provides more information about the bulk density of granular flows entering water than the characteristics of the leading wave alone.

6 Discussion

Pyroclastic density currents impacting a body of water are addressed with the aim of better understanding and predicting tsunami generation during volcanic eruptions near water. In the present study, only the basal concentrated component of pyroclastic density currents, i.e. the pyroclastic flow, is modeled experimentally because it is the main contributor to wave generation, whereas the upper dilute surge is expected to propagate over the water surface (Watts and Waythomas, 2003). By characterizing the properties of waves generated in the near- and far-field regions of the coastline, our results suggest that the bulk density of pyroclastic flows influences the amplitude of the waves, but to a lesser extent than the other flow parameters (i.e., volume, velocity and thickness). This result is in line with those of recent studies on landslide-tsunamis that suggest bulk flow density has a second-order effect on the amplitude of the leading and largest waves generated by fluid (Kriaa et al, 2022) or non-fluidized granular (Robbe-Saule et al, 2021; Nguyen, 2022) columns collapsing into water. Quantitatively, the above-mentioned authors concluded that increasing bulk density by a factor of about ten doubled the maximum amplitude. Previously, Zweifel et al (2006) showed that the bulk density difference between light and heavy coarse-grained flows entering water slightly affected the amplitude of the leading wave (an increase of the amplitude by a factor 1.1 when the bulk density was increased by a factor 1.7, see their Fig. 9), keeping other dimensionless parameters constant.

The present study shows that the far-field amplitude of the leading and largest wave evolves quasi-linearly with the bulk flow density, i.e. $A_{ff} \propto \rho$, like with the other flow parameters according to the scaling of Bougouin et al (2020). Based on this empirical law, the wave amplitude of natural tsunamis is expected to vary by no more than a factor $3-4$ by assuming a maximum particle volume fraction of $0.5-0.6$ and solid particle density not exceeding from 900 to 3000 kg.m^{-3} for natural pyroclastic flows. This contrasts sharply with variations of several orders of magnitude for other flow parameters, which underlines the moderate importance of the bulk flow density in the prediction of volcanic tsunamis. By contrast, we also report a relatively strong influence of the bulk flow density on the properties of the wave train, and thus on the energy distribution between the leading wave and the wave train. However, predicting the amplitude and velocity of the leading wave, that is the first and largest wave to hit the coastline in most cases, remains the real priority for hazard assessment, even though wave trains could become significant in resonance cases. Our results therefore reveal that the knowledge of bulk density for natural pyroclastic flows is of second-order importance for hazard assessment, and we recommend that future studies investigate other flow parameters to assess their respective contribution.

7 Conclusion

In this study, we experimentally investigated the bulk density effect of pyroclastic flows on tsunami generation for improving our knowledge on the main parameters to be taken into account for hazard assessment. We considered both light and heavy, variably fluidized, fine-grained flows down an inclined plane, and then entering a water reservoir. First, general observations on granular flow propagation dynamics and tsunami generation showed that the change in bulk flow density resulted in different dynamics of the subaqueous granular material, which could form either positively- or negatively-buoyant gravity currents below the water surface at early stages. By contrast, the generation process of the leading wave was similar for both flow types. The wave amplitude was initially similar to the local water depth along the inclined plane, and then reached a maximum amplitude dependent on initial parameters, while being moderately affected by the bulk flow density. At longer times and far away from the shoreline, further characterization revealed the physical contribution of the bulk flow density on the amplitude of the leading wave, while other wave features (i.e., period, velocity, asymmetry) remained globally unchanged. Quantitatively, the far-field amplitude of the leading wave evolved quasi-linearly with the bulk flow density, which was fairly well captured by the scaling of Bougouin et al (2020). Finally, the largest effect of the bulk flow density on tsunami generation was reported on the energy distribution between the leading wave and the total wave train, which was attributed to different modes of interaction between light or heavy granular flows and the water. Though bulk flow density must be taken into account to improve physical understanding and modeling of tsunami generation, we conclude that knowledge of this parameter is not critical relative to other flow parameters, such as the velocity, thickness and volume, for tsunami hazard assessment.

Appendix: Other far-field features of the leading wave

We investigated also the effect of the bulk flow density on other characteristics of the leading wave, namely its period T, the propagation velocity c and the asymmetry coefficient A_s of the first positive crest (Fig. 8). As for the far-field amplitude A_{ff} presented in the main text, the values of the period T and the asymmetry coefficient A_s correspond here to measurements made at $x = 2.4$ m (i.e., $x/H_o = 9$) from the shoreline, while the error bars indicate the variation from $x = 2$ to 2.8 m (i.e., from $x/H_o = 7.5$ to 10.5).

Figure 8(a) shows that there are no significant variations on the scaled period $(g/H_o)^{1/2}T = 6$, and propagation velocity $c/(gH_o)^{1/2} = 1$, of the leading wave far away from the shoreline, in the range of parameters considered. To quantify the wave asymmetry coefficient As, the method used by Bullard et al (2019b) is considered, which consists of fitting the temporal evolution of the wave height profile $\eta(x,t)$ over the period T of the leading wave, in a stationary location (i.e., $x = 0$ and $t = 0$ defined as the position and the time at which the far-field amplitude A_{ff} is measured), as

$$\eta(x,t) = A_{ff}\,\mathrm{sech}^2\left[\alpha^{-/+}\sqrt{\frac{3A_{ff}}{4H_o^3}}\,(-ct)\right], \quad (5)$$

where the two fitting parameters α^- and α^+ take a different value on either side of $t = 0$, and the wave velocity is set to $c = (gH_o)^{1/2}$ according to our results [inset of Fig. 8(a)]. Recall also that Eq. 5 is derived from the stationary solitary wave solution that describes a perfectly symmetrical wave with $\alpha^- = \alpha^+ = 1$ (Le Méhauté, 1976). Then, the asymmetry coefficient is estimated as $As = (9/5\pi)\ln(\alpha^+/\alpha^-)$ using the empirical relation proposed by Bullard et al (2019b). In any case, the main purpose of the asymmetry coefficient A_s is to quantify the general shape of waves with three distinct types of asymmetry, namely asymmetry with steeper and flatter front faces for negative and positive values of As, respectively, and symmetrical shape with $As = 0$. The inset

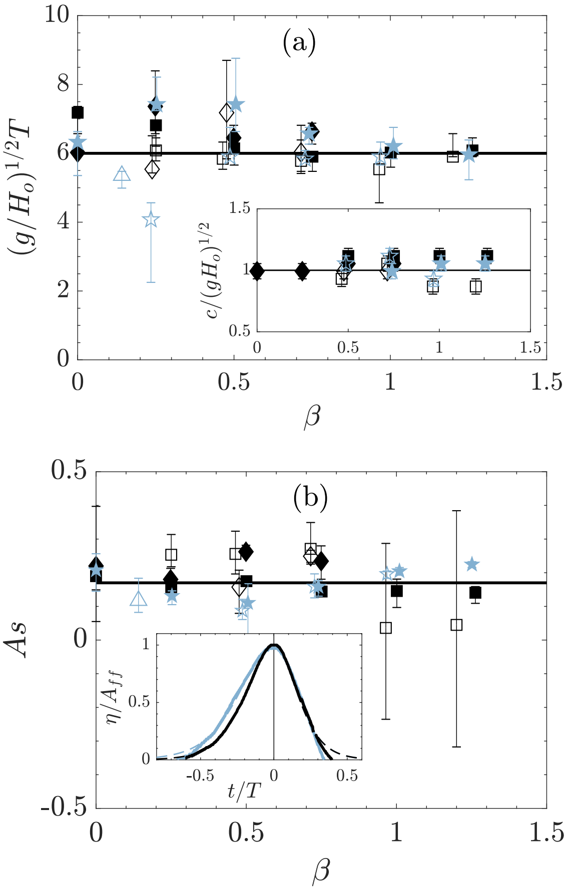

Fig. 8 (a) Scaled period $(g/H_o)^{1/2}T$ (inset: scaled velocity $c/(gH_o)^{1/2}$) and (b) asymmetry coefficient A_s of the leading wave versus the degree of fluidization β. Both T and A_s are estimated at $x = 2.4$m (i.e., $x/H_o = 9$) from the shoreline, while error bars indicate the variation from $x = 2$ to 2.8m (i.e., from $x/H_o = 7.5$ to 10.5). (—) $(g/H_o)^{1/2}T = 6$ (inset: $(c/(gH_o)^{1/2} = 1)$; $A_s = 0.17$ (Average values of data). The bottom inset of Fig. 8(b) shows η/A_{ff} versus t/T (here, $t = 0$ is the time at which A_{ff} is measured) in the far-field, after a light (blue, particles P143) or heavy (dark, particles G66) granular flow ($\beta = 1.3$, $\theta = 30^\circ$) enters water. Dashed lines (visible at small and large t/T) correspond to Eq. 5 with $\alpha^- \sim 1.5$ (blue) and 1.2 (black), for $t/T < 0$, and $\alpha^+ \sim 2.2$ (blue) and 1.5 (black), for $t/T > 0$. Symbols: (□) G66; (◇) G159; (☆) P143; (△) P580, with $\theta = 15^\circ$ (opened) and $\theta = 30^\circ$ (closed).

of Fig. 8(b) reveals a slight asymmetry with the leading edge of the wave that is generally slightly steeper than the trailing edge, while fitting curves (dashed lines) are barely observed due to an excellent agreement with the data. Again, no significant variation in As is reported when varying the bulk flow density (blue vs. black symbols), as well as the degree of fluidization β, which can therefore be characterized by a constant value of $As = 0.17$ [solid line, Fig. 8(b)].

Abbreviations

Abbreviation	Description
g	Gravitational acceleration
x	Horizontal coordinate
t	Time
θ	Slope angle of the inclined plane
H_o	Maximum water height
ρ_w	Water density
L_i	Initial column length
H_i	Initial column height
ϕ_i	Particle volume fraction of initial granular column
V_f	Fluidization velocity
V_{mf}	Minimum fluidization velocity
ρ_p	Particle density
d	Mean particle diameter
α_r	Repose angle of particles
$G66$	Glass beads of $d = 66\,\mu$m
$G159$	Glass beads of $d = 159\,\mu$m
$P143$	Polystyrene beads of $d = 143\,\mu$m
$P580$	Polystyrene beads of $d = 580\,\mu$m
h_l	Height of the granular layer remaining in the reservoir
ρ	Bulk flow density
u_f	Flow-front velocity
u_f^W	Water flow-front velocity
$h(x,t)$	Flow thickness profile
h_f	Flow-front thickness
h_f^W	Water flow-front thickness
v	Volume per unit width
$\eta(x,t)$	Water height elevation
A	Amplitude of the leading wave
A_m	Maximum amplitude
A_{ff}	Far-field amplitude (at $x = 2.4$ m)
x^A	Position of the wave amplitude
T	Leading crest period
c	Wave velocity
A_s	Asymmetry coefficient
$\langle E_w \rangle$	Wave crest energy
E_w	Total wave energy
E_k^f	Kinetic granular flow energy
$\beta = V_f/V_{mf}$	Degree of fluidization
$Fr^f = u_f/(gh_f)^{1/2}$	Flow Froude number
$Fr = u_f/(gH_o)^{1/2}$	Froude number
$S = h_f/H_o$	Relative flow thickness
$R = \rho/\rho_w$	Relative flow density
$V = v/{H_o}^2$	Relative flow volume
$\zeta = FrSRV\sin\theta$	-

Supplementary information. The online version contains a supplementary material available at [XX].

Acknowledgments. The authors acknowledge the technical staff of the Laboratoire Magmas et Volcans for their contribution in designing and constructing the experimental setup. The authors would also like to thank the two referees, Emily Lane and Dave Tappin, as well as the Associate Editor, Tomaso Esposti Ongaro, for their constructive comments, which helped to improve the initial manuscript. This is ClerVolc contribution n°638.

Funding. This work was funded by the ANR RAVEX (ANR-16-CE03-0002) project.

Data availability. All data and materials are available by request to the authors.

Declarations

Conflict of interest. The authors declare no competing interests.

References

Allen SR, Freundt A, Kurokawa K (2012) Characteristics of submarine pumice-rich density current deposits sourced from turbulent mixing of subaerial pyroclastic flows at the shoreline: field and experimental assessment. Bull Volcanol 74:657–675

Blong RJ, McKee CO (1995) The Rabaul eruption 1994 - Destruction of a town. Natural Hazards Research Center, Macquarie University, Sydney

Bougouin A, Paris R, Roche O (2020) Impact of fluidized granular flows into water: Implications for tsunamis generated by pyroclastic flows. J Geophys Res Solid Earth 125:e2019JB018954

Bougouin A, Roche O, Paris R, et al (2021) Experimental insights on the propagation of fine-grained geophysical flows entering water. J Geophys Res Oceans 126:e2020JC016838

Bullard GK, Mulligan RP, Carreira A, et al (2019a) Experimental analysis of tsunamis generated by the impact of landslides with high mobility. Coast Eng 152:103538

Bullard GK, Mulligan RP, Take WA (2019b) An enhanced framework to quantify the shape of impulse waves using asymmetry. J Geophys Res Oceans 124:652–666

Carey S, Sigurdsson H, Mandeville C, et al (1996) Pyroclastic flows and surges over water: an example from the 1883 Krakatau eruption. Bull Volcanol 57:493–511

Carey S, Sigurdsson H, Mandeville C, et al (2000) Volcanic hazards from pyroclastic flow discharge into the sea: examples from the 1883 eruption of Krakatau, Indonesia. Geol Soc Am Spec Publi 345:1–14

Cas RAF, Wright JV (1991) Subaqueous pyroclastic flows and ignimbrites: an assessment. Bull Volcanol 53:357–380

Casalbore D, Di Traglia F, Romagnoli C, et al (2022) Integration of remote sensing and offshore geophysical data for monitoring the short-term morphological evolution of an active volcanic flank: a case study from stromboli island. Remote Sens 14:4605

Clous L, Abadie S (2019) Simulation of energy transfers in waves generated by granular slides. Landslides 16:1663–1679

Day SJ (2015) Volcanic tsunamis. In: The Encyclopedia of Volcanoes. Academic Press, Amsterdam

Delannay R, Valance A, Mangeney A, et al (2017) Granular and particle-laden flows: from laboratory experiments to field observations. J Phys D 50:053001

Dufek J (2016) The fluid mechanics of pyroclastic density currents. Ann Rev Fluid Mech 48:459–485

Freundt A (2003) Entrance of hot pyroclastic flows into the sea: Experimental observations. Bull Volcanol 65:144–164

Fritz HM, Hager WH, Minor HE (2004) Near field characteristics of landslide generated impulse waves. J Waterway, Port, Coast Ocean Eng 130:287–302

Giordano G, De Astis G (2021) The summer 2019 basaltic Vulcanian eruptions (paroxysms) of Stromboli. Bull Volcanol 83:1–27

Heller V, Hager WH (2010) Impulse product parameter in landslide generated impulse waves. J Waterway, Port, Coast Ocean Eng 136:145–155

Jutzeler M, Marsh R, Carey RJ, et al (2014) On the fate of pumice rafts formed during the 2012 Havre submarine eruption. Nat Commun 5:3660

Kriaa Q, Viroulet S, Lacaze L (2022) Modeling of impulse waves generated by a viscous collapse in water. Phys Rev Fluids 7:054801

Le Méhauté B (1976) An introduction to hydrodynamics and water waves. Springer–Verlag, New York

Lee CH, Huang Z (2021) Effects of grain size on subaerial granular landslides and resulting impulse waves: experiments and multi-phase flow simulation. Landslides 19:137–153

Legros F, Druitt TH (2000) On the emplacement of ignimbrite in shallow-marine environments. J Volcanol Geotherm Res 95:9–22

Lipiejko N, Whittaker CN, Lane EM, et al (2022) Experimental modeling of tsunamis generated by pyroclastic density currents: The effects of particle size distribution on wave generation. J Geophys Res Solid Earth 127:e2022JB024847

Lipiejko N, Whittaker CN, Lane EM, et al (2023) Wave generation by fluidized granular flows: Experimental insights into the maximum near-field wave amplitude. J Geophys Res Oceans 128:e2022JC019583

Maeno F, Imanura F (2011) Tsunami generation by a rapid entrance of pyroclastic flow into the sea during the 1883 Krakatau eruption, Indonesia. J Geophys Res 116:B09205

Mattioli GS, Voight B, Linde AT, et al (2007) Unique and remarkable dilatometer measurements of pyroclastic flow–generated tsunamis. Geology 35:25–28

Milner DM, Cole JW, Wood CP (2003) Mamaku ignimbrite: a caldera-forming ignimbrite erupted from a compositionally zoned magma chamber in Taupo volcanic zone, New Zealand. J Volcanol Geotherm Res 122:243–264

Nguyen NHT (2022) Collapse of partially and fully submerged granular column generating impulse waves: An empirical law of maximum wave amplitude based on coupled multiphase fluid-particle modeling results. Phys Fluids 34:013309

Nishimura Y, Nakagawa M, Kuduon J, et al (2005) Timing and scale of tsunamis caused by the 1994 Rabaul eruption, East New Britain, Papua New Guinea. In: Tsunamis: Case Studies and Recent Developments. Springer, Dordrecht

Nomikou P, Druitt TH, Hübscher C, et al (2016) Post-eruptive flooding of Santorini caldera and implications for tsunami generation. Nat Commun 7:13332

Paris R (2015) Source mechanisms of volcanic tsunamis. Phil Trans R Soc A 373:20140380

Paris R, Wassmer P, Lavigne F, et al (2014) Coupling eruption and tsunami records: the Krakatau 1883 case-study, Indonesia. Bull Volcanol 76:1–23

Pelinovsky E, Zahibo N, Dunkley P, et al (2004) Tsunami generated by the volcano eruption on July 12–13, 2003 at Montserrat, Lesser Antilles. Sci Tsunami Hazards 22:44–57

Robbe-Saule M, Morize C, Henaff R, et al (2021) Experimental investigation of tsunami waves generated by granular collapse into water. J Fluid Mech 907:A11

Roche O, Montserrat S, Niño Y, et al (2008) Experimental observations of water-like behavior of initially fluidized, dam break granular flows and their relevance for the propagation of ash-rich pyroclastic flows. J Geophys Res 113:B12203

Schumacher R, Mues-Schumacher U (1996) The Kizilkaya ignimbrite - an unusual low-aspect-ratio ignimbrite from Cappadocia, central Turkey. J Volcanol Geotherm Res 70:107–121

Sulpizio R, Dellino P, Doronzo DM, et al (2014) Pyroclastic density currents: state of the art and perspectives. J Volcanol Geotherm Res 283:36–65

Viroulet S, Sauret A, Kimmoun O (2014) Tsunami generated by a granular collapse down a rough inclined plane. Europhys Lett 105:34004

Watts P, Waythomas CF (2003) Theoretical analysis of tsunami generation by pyroclastic flows. J Geophys Res 108:2563–2583

Zitti G, Ancey C, Postacchini M, et al (2016) Impulse waves generated by snow avalanches: Momentum and energy transfer to a water body. J Geophys Res Earth Surface 121:2399–2423

Zweifel A, Hager H, Minor HE (2006) Plane impulse waves in reservoirs. J Waterway, Port, Coast Ocean Eng 132:356–368